Particuology 109 (2026) 211–218

Contents lists available at ScienceDirect

Particuology

journal homepage: www.elsevier.com/locate/partic

MXene-assisted NiFe sulfides with interfacial modulation for oxygen evolution electrocatalysis

Pei-Wei Zhong[1], Hong-Xiao Yang[1], Wenkang Xu, Zhiyang Yu, Bei Li, Hongjuan Wang, Yonghai Cao, Hao Yu, Hao-Fan Wang[*]

School of Chemistry and Chemical Engineering, South China University of Technology, Guangzhou, 510641, Guangdong, China

HIGHLIGHTS

- A core–shell S-NiFc MOF@Mo_2CT_x MXene hybrid was synthesized via a facile two-step hydrothermal strategy.
- Strong interfacial coupling between sulfides and MXene promotes efficient electron redistribution and charge transfer.
- Composite catalyst achieves an ultralow overpotential of 223 mV at 10 mA cm^{-2} and a Tafel slope of 41.3 mV dec^{-1}.
- This study expands application scope of MXenes and provides new insights into optimizing OER electrocatalysts.

GRAPHICAL ABSTRACT

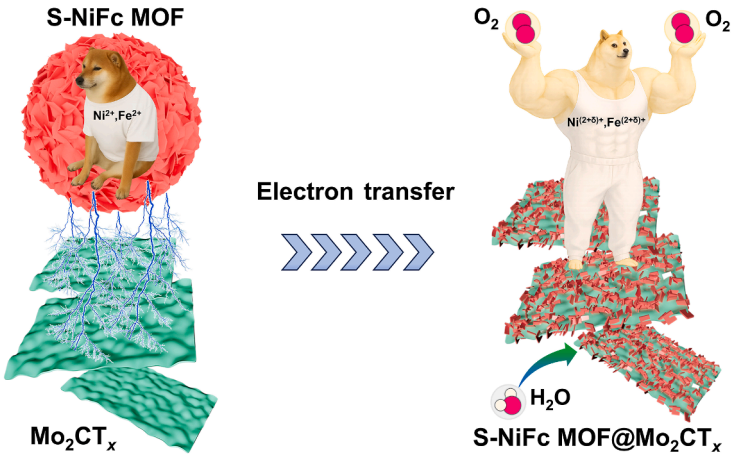

ARTICLE INFO

Keywords:
Oxygen evolution reaction
Electrocatalyst
Transition-metal-based materials
NiFe sulfides
Mo_2CT_x MXene

ABSTRACT

Oxygen evolution reaction (OER) plays a vital role in various pivotal electrochemical applications. To improve the energy efficiency and economic viability of these technologies, it is critical to develop cost-effective and highly active OER electrocatalysts based on earth-abundant elements. Among various candidates, transition-metal-based compounds have demonstrated notable potential for OER electrocatalysis, attributable to their adjustable electronic configurations. Nevertheless, their practical application remains constrained by limited intrinsic activity, poor electrical conductivity, and particle aggregation, which compromise their overall OER efficiency. In this study, an efficient OER electrocatalyst, S-NiFc MOF@Mo_2CT_x, is constructed by the sulfidation of NiFe-based metal–organic framework (MOF) precursors anchored on conductive Mo_2CT_x MXene. The MOF-derived NiFe sulfides offer abundant accessible active sites, and the strong interfacial coupling between NiFe sulfides and Mo_2CT_x enhances the catalyst's intrinsic activity. The conductive Mo_2CT_x matrix also guarantees

This article is part of a special issue entitled: SI honoring Profs. Jin & Yu published in Particuology.

* Corresponding author.
E-mail address: whf@scut.edu.cn (H.-F. Wang).

[1] These authors contributed equally to this work.

https://doi.org/10.1016/j.partic.2025.12.020
Received 21 November 2025; Received in revised form 19 December 2025; Accepted 20 December 2025
Available online 2 January 2026

1674-2001/© 2026 Chinese Society of Particuology and Institute of Process Engineering, Chinese Academy of Sciences. Published by Elsevier B.V. All rights are reserved, including those for text and data mining, AI training, and similar technologies.

efficient electron transport and homogeneous dispersion of the active phase. As a result, S-NiFc MOF@ Mo_2CT_x exhibits excellent OER activity, reaching 10 mA cm^{-2} at an overpotential of 223 mV, along with stable operation for 68 h in 1.0 M KOH solution. This study broadens the scope of MXene-based materials in electrocatalytic applications and offers valuable insights into optimizing NiFe-derived OER catalysts.

1. Introduction

In the global pursuit of sustainable and carbon-neutral energy, hydrogen plays a vital role as a clean fuel with high energy density (Gao et al., 2024; Qi et al., 2018; Sun et al., 2024; Wu et al., 2022). Among various hydrogen production technologies, water electrolysis stands out as an environmentally friendly method to generate high-purity hydrogen, with strong potential for integration with renewable energy sources such as solar and wind power (Ali & Shen, 2020; Liu et al., 2025; Wu et al., 2025; Zhang, Zou, et al., 2024). However, the efficiency of water electrolysis is primarily limited by the sluggish kinetics of the oxygen evolution reaction (OER) at the anode (Han et al., 2024; Pazhamalai et al., 2024). This complex four-electron process involves multiple intermediates and requires a high overpotential, making it the key bottleneck for both the efficiency and stability of water electrolysis systems (Abdelrahim et al., 2023; Gultom et al., 2023). Therefore, the rational design of high-performance OER electrocatalysts that accelerate kinetics while reducing overpotential is of great significance for improving the economic feasibility of electrolysis-based hydrogen production (Li et al., 2023; Qiu et al., 2022).

Precious metal oxides like IrO_2 and RuO_2 have long been the benchmark OER electrocatalysts due to their excellent activity and durability (Xie et al., 2023; Zhu et al., 2024). However, their high cost and scarcity limit large-scale application (Shi et al., 2025). This has driven research towards developing cost-effective, earth-abundant non-precious metal catalysts with comparable performance (Li et al., 2023; Sondermann et al., 2022; Zong et al., 2021).

Transition metal-based materials (TMMs) are promising candidates because of their abundance, low cost, and tunable electronic properties (Li et al., 2021; Radwan et al., 2021). In particular, NiFe-based catalysts show excellent activity and corrosion resistance in alkaline media due to synergistic electronic effects (Kim et al., 2018; Zhuo et al., 2023). However, their practical use is hindered by poor conductivity and particle agglomeration, which inhibit electron transfer and mass transport during electrocatalysis (Meng et al., 2024; Qi et al., 2024). Metal–organic frameworks (MOFs), with their ordered porous architecture and plentiful metal active sites, have emerged as promising precursors that help improve the reactant accessibility, thereby mitigating the intrinsic limitations of traditional TMMs (Ji et al., 2022; Liu et al., 2023; Nozari-Asbemarz et al., 2025). MOF-derived TMMs inherit these features, significantly enhancing catalytic performance (Gaba et al., 2024). Moreover, heteroatom doping via sulfidation can effectively modulate the electronic structure of the catalyst, thereby optimizing reaction kinetics and facilitating the formation of transition metal sulfides (TMSs) with abundant active sites (Wang et al., 2019a, 2019b, 2024; Zhao et al., 2022). Despite these advances, MOF-derived TMSs still suffer from limited conductivity and structural instability under prolonged electrolysis (Kundu et al., 2023; Xing et al., 2024; Zhong et al., 2022). To address these issues, constructing composite systems with conductive supports has proven to be an effective strategy for improving the electron transport capabilities and durability of MOF-derived TMSs.

Two-dimensional transition metal carbides and nitrides, known as MXenes, have emerged as ideal conductive substrates due to their high electrical conductivity, large specific surface area, and abundant surface functional groups (Shahzad et al., 2020; Zhang, Zou, et al., 2024). Titanium carbide ($Ti_3C_2T_x$) MXene is widely studied (Ahn et al., 2020; Salles et al., 2019); however, its surface is prone to oxidation in alkaline environments, which compromises its catalytic activity and stability (Krämer et al., 2024; Tang et al., 2019). Additionally, the limited variety of surface functional groups restricts its integration with active components (Guo et al., 2025; Tang et al., 2022). In contrast, molybdenum carbide (Mo_2CT_x) MXene exhibits superior chemical stability and tunable surface chemistry (Loupias et al., 2024; Unnikrishnan et al., 2022), which serve as ideal platforms for supporting active materials and facilitating electron transport (Liu et al., 2021; Peng et al., 2021). Furthermore, its mechanical flexibility helps mitigate structural degradation caused by volume changes during electrolysis (Liu et al., 2024). Integrating Mo_2CT_x with MOF-derived TMSs offers multiple benefits, including robust support, efficient electron transport, suppression of active component agglomeration, and strong interfacial interactions that induce electronic structure rearrangement, thereby optimizing reaction kinetics and enhancing both activity and durability. As such, the design of Mo_2CT_x-based composites with MOF-derived TMSs presents a promising and innovative route for constructing efficient and stable non-precious metal OER electrocatalysts.

In this study, a facile two-step hydrothermal strategy was employed to successfully synthesize the composite electrocatalyst S-NiFc MOF@-Mo_2CT_x, which integrates the abundant active sites of MOF-derived NiFe sulfides with the superior electronic conductivity of Mo_2CT_x MXene. The sulfidation process introduces a high density of active sites while preserving the porous structure, thereby promoting reactant diffusion and active site exposure. Through strong interfacial coupling, Mo_2CT_x facilitates efficient electron transfer between the sulfides and the carbide, significantly optimizing the electronic structure and reaction kinetics. This composite catalyst demonstrates remarkable OER performance in alkaline media, featuring a low overpotential of 223 mV at 10 mA cm^{-2}, a Tafel slope of only 41.3 mV dec^{-1}, and stable current density after continuous operation of 68 h, clearly outperforming its single-component counterparts. This work not only presents a MOF-derived sulfide/MXene OER electrocatalyst with improved charge transport and structural robustness, but also provides a viable design strategy for advanced non-precious metal OER electrocatalysts, expanding the application potential of MOF-derived sulfide/MXene composites in energy conversion technologies.

2. Experimental

2.1. Synthesis of NiFc MOF@Mo_2CT_x

10 mg of Mo_2CT_x MXene and 0.0625 mmol of $NiCl_2$ were added to 5 mL of deionized water and ultrasonicated for 3 min to ensure homogeneous dispersion. Meanwhile, 0.0625 mmol of 1,1′-ferrocenedicarboxylic acid (Fc) was dissolved in 10 mL of N,N-dimethylformamide (DMF). The two solutions were then transferred into a Teflon-lined autoclave and heated at 125 °C for 12 h. After the reaction, the resulting precipitate was collected by centrifugation and washed three times with ethanol and distilled water. Finally, the product was freeze-dried to obtain a dark yellow precipitate, denoted as NiFc MOF@Mo_2CT_x. The synthesis of NiFc MOF follows the same procedure as outlined in Section 2.1, with the omission of Mo_2CT_x from the reaction system. Details regarding the preparation of Mo_2CT_x can be found in supplementary Text S2.

2.2. Synthesis of S-NiFc MOF@Mo_2CT_x

10 mg of NiFc MOF@Mo_2CT_x and 0.32 g of thioacetamide (TAA) were dispersed in 48 mL of anhydrous ethanol and ultrasonicated in a beaker for 3 min to ensure uniform mixing. The resulting mixture was

then subjected to a solvothermal reaction at 140 °C for 6 h. The obtained precipitate was washed three times with distilled water and anhydrous ethanol. Finally, the precipitate was freeze-dried to yield a black powder, denoted as S-NiFc MOF@Mo_2CT_x. The synthesis of S-NiFc MOF follows the same procedure as outlined in Section 2.2, with the omission of Mo_2CT_x from the reaction system.

2.3. Electrochemical measurements

All electrochemical measurements were performed at room temperature in a 1.0 M KOH electrolyte that had been purged with high-purity argon gas. A conventional three-electrode system was employed throughout the tests. Details regarding sample preparation and preconditioning procedures are provided in the supplementary data (Text S3). Following each experiment, electrode potentials were recalculated relative to the reversible hydrogen electrode (RHE) using the formula: $E_{RHE} = E_{Hg/HgO} + E_{CAL}$, where $E_{Hg/HgO}$ represents the potential recorded versus the Hg/HgO reference, and E_{CAL} denotes the experimentally determined calibration offset between the Hg/HgO and RHE. To assess the oxygen evolution performance, linear sweep voltammetry (LSV) was carried out at a scan velocity of 5 mV s^{-1}. All reported overpotential values were corrected for ohmic losses through the relationship: $E_{corrected} = E_{measured} - 95\% iR_{solution}$, with $R_{solution}$ representing the solution resistance, which was determined by electrochemical impedance spectroscopy (EIS) at 1.5 V vs. RHE. The kinetic behavior was further elucidated by applying the Tafel model: $\eta = a + b \log j$, in which b denotes the Tafel slope and j the current density. Impedance spectra were acquired using an AC perturbation of 5 mV amplitude over a frequency interval spanning from 100 kHz to 0.01 Hz, enabling the extraction of both charge transfer resistance and solution resistance. To evaluate electrocatalyst durability under accelerated aging conditions, cyclic voltammetry (CV) was continuously performed within a voltage range of 0–0.4 V (vs. RHE) at a sweep rate of 100 mV s^{-1}. In parallel, long-term operational stability was investigated using chronoamperometric (CA) or chronopotentiometric (CP) methods by maintaining either a constant potential or fixed current density, respectively. The electrochemical surface area (ECSA) was approximated through the determination of double-layer capacitance (C_{dl}), which was extracted from CV profiles acquired in a non-Faradaic potential window at various scan rates ranging from 10 to 100 mV s^{-1}. The charging current (i_{dl}) was calculated as the half-difference between anodic and cathodic currents: $i_{dl} = 0.5 (i_{anode} - i_{cathode})$. Subsequently, C_{dl} was determined from the slope of the i_{dl} versus scan rate plot. Assuming a specific capacitance (C_s) of 0.04 mF cm^{-2} typical for a flat electrode surface, ECSA was then computed using the expression: ECSA $= C_{dl}/C_s$ (Kim et al., 2024; McCrory et al., 2013; Mohideen et al., 2026; Quiroz et al., 2025).

3. Results and discussion

The synthetic procedure of the S-NiFc MOF@Mo_2CT_x heterostructure is illustrated in Fig. 1. To construct this heterostructure, $NiCl_2$ and the Fc ligand were mixed with MXene nanosheets and subjected to a solvothermal reaction, enabling the in situ growth of NiFc MOF on the surface of Mo_2CT_x. Subsequently, TAA was introduced as the sulfur source in a hydrothermal process to obtain the final S-NiFc MOF@-Mo_2CT_x material.

The synthesis of Mo_2CT_x MXene was conducted using the "sweet" solvothermal etching method previously reported by our research group (Xu et al., 2024). In this approach, glycerol serves as the reaction medium, enabling mild and selective etching of the MAX-phase precursor. The synthesis route of the obtained MXene is provided in Text S2.

To gain a deeper understanding of the formation mechanism of Mo_2CT_x MXene, we systematically investigated its morphological evolution using scanning electron microscopy (SEM). As shown in Fig. 2(a), the pristine Mo_2Ga_2C MAX phase exhibits a dense bulk structure with a smooth surface and well-defined edges. After treatment via the "sweet" method, the Ga layers within the MAX phase are selectively removed, yielding a multilayer Mo_2C intermediate with a characteristic accordion-like morphology (Fig. 2(b)). To achieve effective delamination of the layered structure, the intermediate was further treated with tetramethylammonium hydroxide (TMAOH) as an intercalating agent. The TMA^+ ions, through ion exchange, were inserted between the Mo_2C layers, effectively weakening the interlayer van der Waals forces. As shown in Fig. 2(c), the resulting Mo_2CT_x MXene nanosheets exhibit a translucent, gauze-like morphology with nanometer-scale thickness and lateral dimensions extending to several micrometers, indicating the successful transformation into few-layer two-dimensional (2D) nanosheets. Further structural characterizations corroborated the observed morphological evolution. X-ray diffraction (XRD) analysis (Fig. 2(d)) revealed the complete disappearance of characteristic diffraction peaks of the original MAX phase, indicating full disruption of its layered structure. Meanwhile, a new diffraction peak corresponding to the (0 0 2) plane of Mo_2CT_x MXene emerged at 6.43°. In addition to the XRD results, EDX mapping of ML-Mo_2C MXene (Fig. 2(e)) and the elemental analysis in Supplementary Tables S1 and S2 provide further evidence that the Ga layers were fully etched from the MAX phase. The oxygen signal is attributed to surface oxygen terminations, while the chlorine signal is ascribed to residual HCl introduced during the acid etching process. These results collectively confirm the successful synthesis of Mo_2CT_x MXene with a well-defined 2D layered structure and surface termination.

The microstructures of NiFc MOF@Mo_2CT_x and S-NiFc MOF@-Mo_2CT_x composites were characterized by SEM. Owing to the self-assembly of microsheets, the NiFc MOF exhibits a flower-like

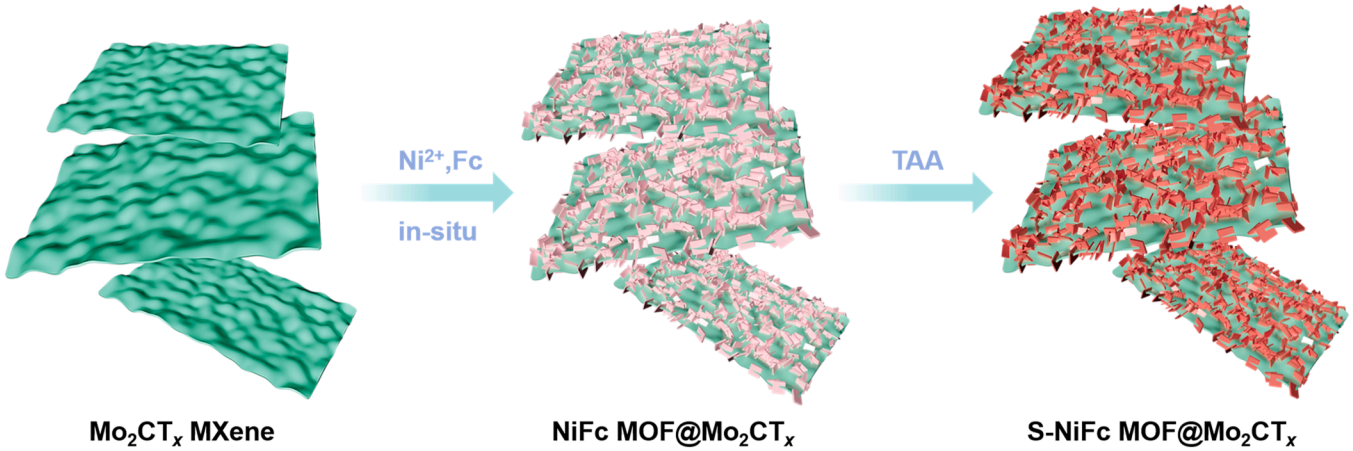

Fig. 1. Schematic illustration of the synthesis process of S-NiFcMOF@Mo_2CT_x.

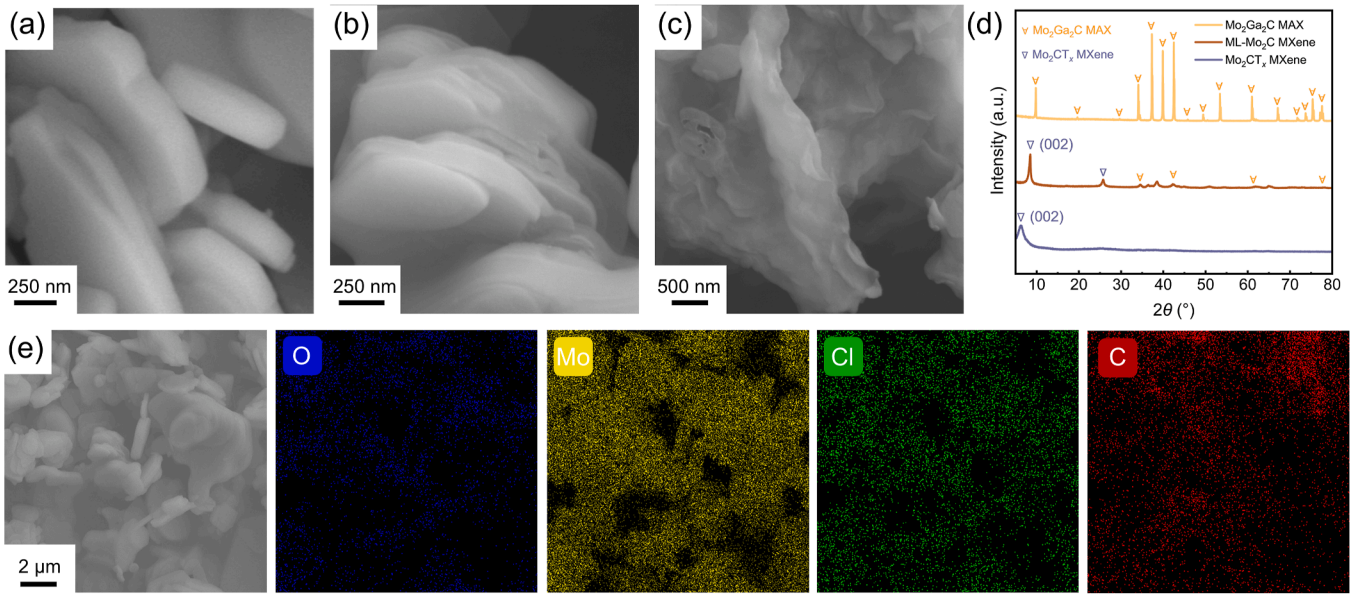

Fig. 2. SEM images of (a) Mo_2Ga_2C MAX, (b) multi-layer Mo_2C MXene (ML-Mo_2C MXene) and (c) few-layer Mo_2C MXene (Mo_2CT_x MXene). This set of images shows the transformation of the precursor MAX phase into Mo_2CT_x MXene through etching and exfoliation. (d) XRD patterns of the crystal structures of Mo_2Ga_2C MAX, ML-Mo_2C MXene and Mo_2CT_x MXene. (e) SEM and EDX mapping images of ML-Mo_2C MXene.

morphology (Fig. 3(a)). EDX mapping reveals uniform distributions of Ni, Fe, Mo, and O elements, indicating the homogeneous dispersion of NiFc MOF within the heterostructure. After sulfur doping, the resulting S-NiFc MOF@Mo_2CT_x largely retains the flower-like morphology of the original NiFc MOF, despite a rougher surface. This two-dimensional nanosheet architecture not only provides abundant active sites but also facilitates the release of large gas bubbles during the OER process, thereby enhancing electrocatalytic performance. The EDX mapping in Fig. 3(b) further confirms the successful incorporation and uniform distribution of S, along with Ni, Fe, and Mo, on the surface of the heterostructure.

Transmission electron microscopy (TEM) was further employed to examine the structure and morphology of S-NiFc MOF@Mo_2CT_x. As shown in Fig. 3(c), NiFc MOF grows around the Mo_2CT_x core, which effectively prevents the spontaneous restacking of Mo_2CT_x and ensures full exposure of the Ni and Fe active centers in the electrolyte. The high-resolution TEM (HRTEM) image in Fig. 3(d) reveals nanosheet structures with an average thickness of approximately 10 nm. HRTEM images in Fig. 3(e) and (f) exhibit a lattice spacing of 0.28 nm, which is indexed to the (1 1 0) crystal plane of Ni_3S_2, demonstrating the presence of the sulfide phase after sulfur treatment. Collectively, the SEM and TEM results demonstrate the successful synthesis of metal sulfides derived from

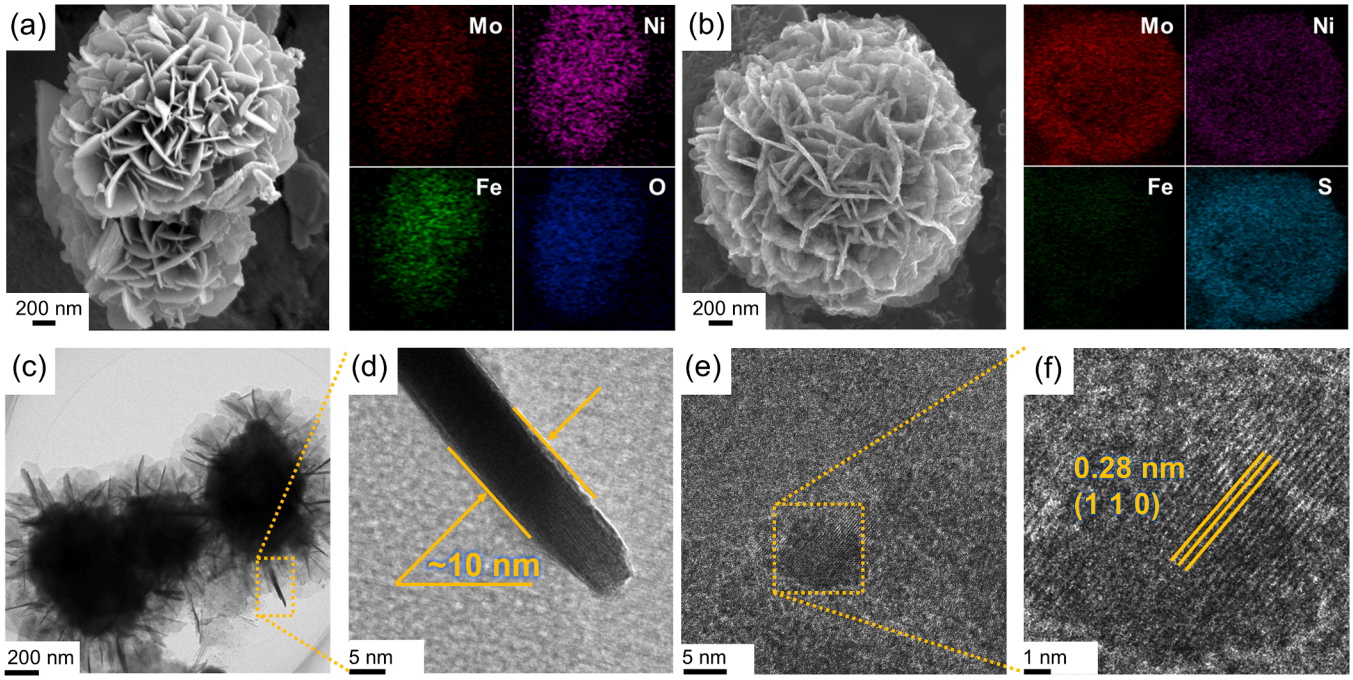

Fig. 3. (a) SEM and EDX images of NiFc MOF@Mo_2CT_x. (b) SEM and EDX mapping images of S-NiFc MOF@Mo_2CT_x. (c) TEM, (d–f) HRTEM images of S-NiFc MOF@Mo_2CT_x.

MOF grown on Mo_2CT_x through a two-step hydrothermal strategy.

The crystal structure of the material was confirmed via XRD analysis, with the experimentally obtained diffraction patterns matching well with literature data shown in Text S5. As depicted in the XRD spectra in Fig. 4(a), for Mo_2CT_x-containing products (NiFc MOF@Mo_2CT_x and S-NiFc MOF@Mo_2CT_x), a diffraction peak corresponding to the (0 0 2) plane of Mo_2CT_x appears in the sample, confirming the successful incorporation of the MXene phase. In the case of S-NiFc MOF@Mo_2CT_x, the diffraction peaks at 39.1° and 54.1° correspond to the (4 0 0) and (4 4 0) planes of Ni_3S_4, respectively, while the peaks at 31.7° and 45.7° are assigned to the (1 1 0) and (2 0 2) planes of Ni_3S_2. Meanwhile, the diffraction signals of the NiFc MOF become markedly weakened, indicating that a portion of the MOF framework is converted into sulfides during the sulfurization process. These results collectively indicate the successful construction of the S-NiFc MOF@Mo_2CT_x composite material.

The chemical composition of S-NiFc MOF@Mo_2CT_x was further characterized by FTIR spectroscopy. As shown in Fig. 4(b), the characteristic peak labeled as 3 at 1670 cm^{-1}, corresponding to the C=O stretching vibration of the −COOH group in the ferrocene dicarboxylic acid moiety, nearly disappears in all three samples (NiFc MOF, NiFc MOF@Mo_2CT_x, and S-NiFc MOF@Mo_2CT_x). The peak 4 at 1560 cm^{-1} corresponds to a new C=O stretching band, corresponding to the formation of $-COO^-$, suggesting successful coordination between Ni^{2+} and the carboxyl groups of the Fc units. In NiFc MOF@Mo_2CT_x and S-NiFc MOF@Mo_2CT_x, the peak 9 at 979 cm^{-1} corresponds to Mo−O, confirming the presence of Mo_2CT_x MXene. Additionally, the peak 11 at 619 cm^{-1} in S-NiFc MOF@Mo_2CT_x corresponds to Ni−S, verifying successful sulfur doping. Other FTIR band assignments are summarized in Table S3 (Liang et al., 2021).

X-ray photoelectron spectroscopy (XPS) was employed to analyze the elemental composition and valence states of S-NiFc MOF@Mo_2CT_x. As shown in Fig. 4(c), compared to NiFc MOF, both NiFc MOF@Mo_2CT_x and S-NiFc MOF@Mo_2CT_x exhibit a Mo peak near 232.5 eV, affirming the presence of Mo_2CT_x. Moreover, the S 2*p* peak appearing around 163.7 eV in S-NiFc MOF@Mo_2CT_x, which is absent in NiFc MOF@Mo_2CT_x, confirms successful sulfur incorporation. As shown in Supplementary Fig. S2, the S 2*p* spectrum can be deconvoluted into a main peak from S^{2-} in M–S bonds and a weaker peak from S−O species, resulting from unavoidable slight surface oxidation. High-resolution Fe 2*p* and Ni 2*p* spectra (Fig. 4(d) and (e)) reveal peaks at 708.4 and 721.1 eV, corresponding to Fe^{2+} $2p_{3/2}$ and Fe^{2+} $2p_{1/2}$ in the Fc units, respectively. Peaks at 856.0 eV ($2p_{3/2}$) and 873.7 eV ($2p_{1/2}$) are associated with Ni^{2+} coordinated with the carboxyl oxygen of Fc. Compared to NiFc MOF, both the Fe and Ni main peaks in S-NiFc MOF@Mo_2CT_x shifted to higher binding energies by 0.21 eV and 0.30 eV, respectively. These results indicate electron withdrawal from the active Fe and Ni centers due to the synergistic effects of Mo_2CT_x support and sulfur doping, which results in their increased valence states. The Mo 3*d* spectrum of S-NiFc MOF@Mo_2CT_x (Fig. 4(f)) displays a distinct change compared with NiFc MOF@Mo_2CT_x. After sulfur incorporation, the relative proportion of Mo^{5+} decreases while Mo^{4+} increases, indicating partial reduction of Mo species. In addition, a new feature assigned to the S 2*s* state appears and overlaps with the Mo 3*d* region, further confirming the successful sulfur doping and the resulting modulation of the electronic structure. On this basis, it can be further concluded that Mo_2CT_x serves as an efficient electron-accepting scaffold, facilitating electron transfer from Fe and Ni to Mo. This electron redistribution leads to an increase in the valence states of the active metal centers. The elevated oxidation states not only enhance orbital hybridization between the metal 3*d* and oxygen 2*p* orbitals, thereby reinforcing metal–oxygen covalency and improving structural stability, but also reduce the energy barrier for metal oxidation during the OER, thus accelerating the reaction kinetics.

Following structural characterization, the OER electrocatalytic performance of the catalysts was systematically investigated. Prior to activity evaluation, CV activation was carried out to stabilize the catalyst surface and ensure reproducible electrochemical behavior. The initial OER activity before activation is relatively low and reaches a stable state after CV cycling (Fig. S3 and Table S4). All subsequent electrochemical

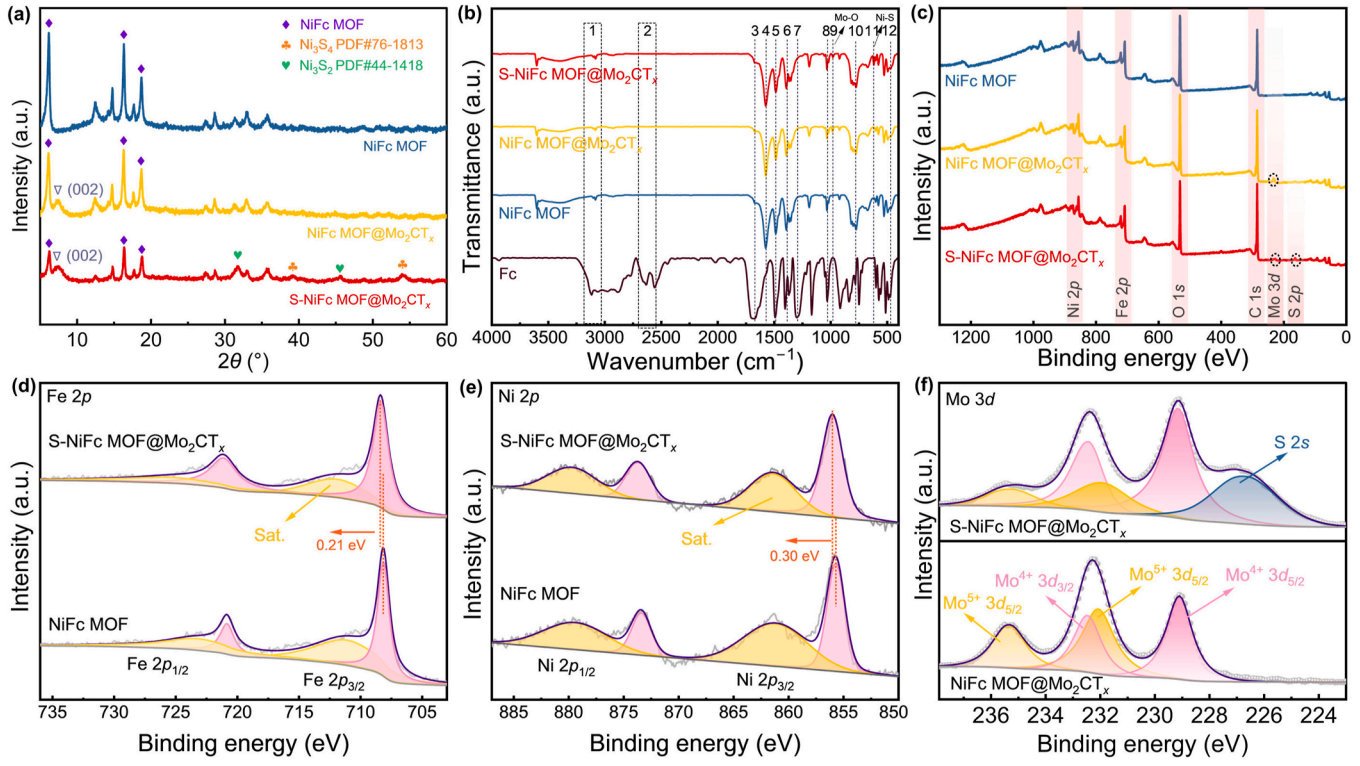

Fig. 4. Structural characterizations of as-prepared samples. (a) XRD patterns. (b) FTIR spectra. (c) XPS survey spectra. (d) Fe 2*p*, (e) Ni 2*p* and (f) Mo 3*d* high-resolution XPS spectra.

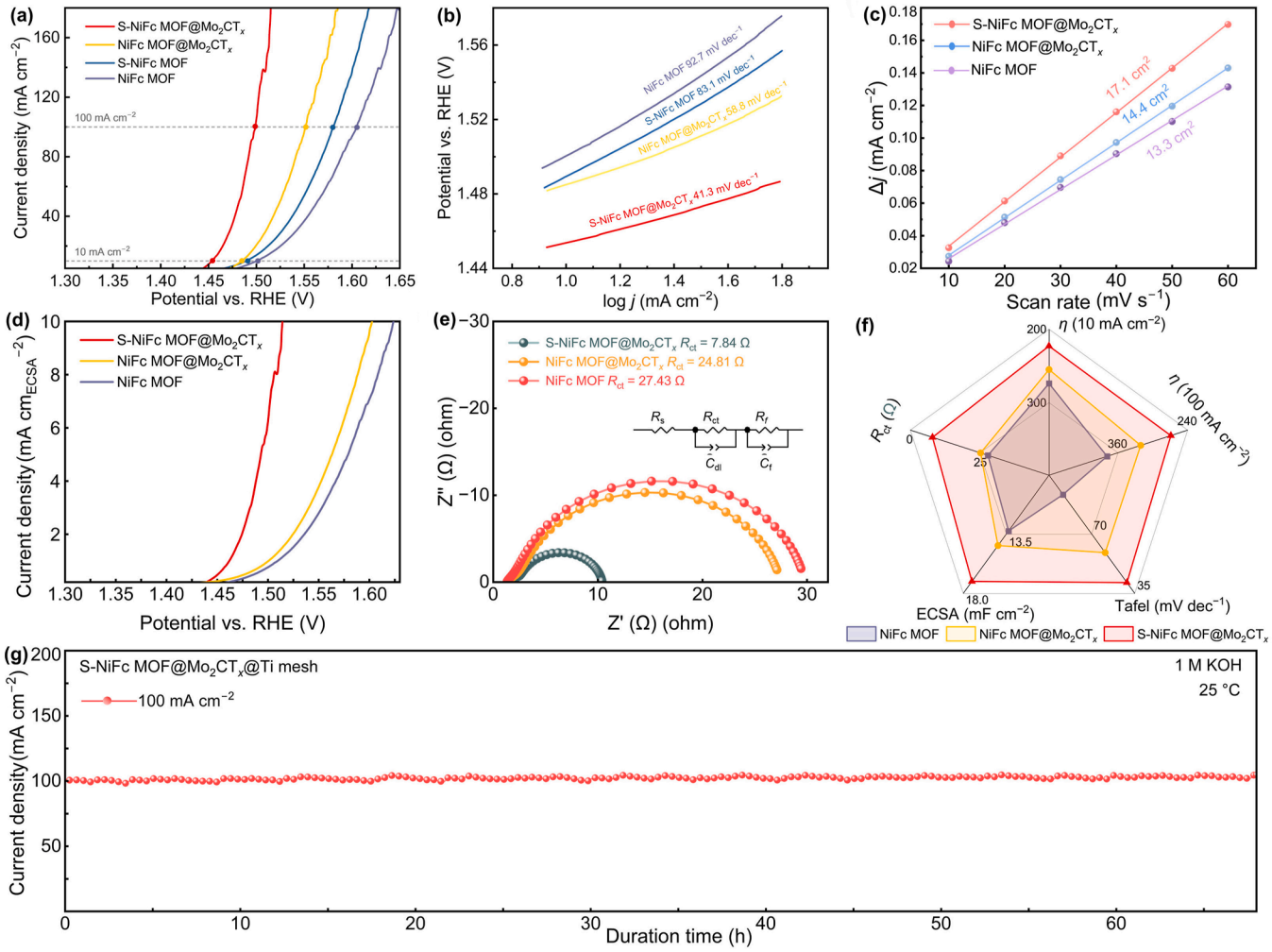

Fig. 5. (a) LSV curves of various catalyst samples, including NiFc MOF, S-NiFc MOF, NiFc MOF@Mo_2CT_x, and S-NiFc MOF@Mo_2CT_x, measured in 1 M KOH. (b) Tafel plots derived from the corresponding LSV curves. (c) ECSA. (d) Current density normalized to ECSA. (e) EIS spectra and (f) Radar chart comparing the key OER performance metrics of NiFc MOF, NiFc MOF@Mo_2CT_x, and S-NiFc MOF@Mo_2CT_x. (g) Chronoamperometric (*i*–*t*) curve of S-NiFc MOF@Mo_2CT_x at an initial current density of 100 mA cm^{-2}.

measurements were conducted on activated samples. As shown in Fig. 5 (a), the linear sweep voltammetry (LSV) curve indicates that S-NiFc MOF@Mo_2CT_x exhibits the lowest overpotential of only 223 mV at an OER current density of 10 mA cm^{-2}, outperforming NiFc MOF@Mo_2CT_x (255 mV), S-NiFc MOF (260 mV), and NiFc MOF (274 mV). Notably, at a high current density of 100 mA cm^{-2}, S-NiFc MOF@Mo_2CT_x still maintains a low overpotential of 269 mV, which is significantly lower than those of the other catalysts (321, 351, and 379 mV, respectively). Tafel slopes derived from the LSV curves are shown in Fig. 5(b). S-NiFc MOF@Mo_2CT_x exhibits the smallest Tafel slope of 41.3 mV dec^{-1}, much lower than those of NiFc MOF (92.7 mV dec^{-1}), S-NiFc MOF (83.1 mV dec^{-1}), and NiFc MOF@Mo_2CT_x (58.8 mV dec^{-1}), suggesting that S-NiFc MOF@Mo_2CT_x possesses the fastest reaction kinetics. In terms of two key catalytic performance indicators, the overpotential at specific current density and the Tafel slope, S-NiFc MOF@Mo_2CT_x surpasses most previously reported NiFc-based powder OER catalysts (see Table S5). This superior performance can be attributed to three factors: (1) the synergistic effects of ferrocene ligands, Mo_2CT_x substrate, and sulfur doping, which facilitate electron transfer from the active Ni sites to the support (Connelly & Geiger, 1996; Lennox et al., 2018); (2) the unique 2D nanosheet morphology of S-NiFc MOF@Mo_2CT_x, which allows for greater exposure of active Ni sites; and (3) the formation of a strong charge-conductive interface between the NiFc MOF and the Mo_2CT_x MXene substrate.

To further evaluate the electrochemical surface properties, CV scans were conducted at different scan rates in the non-Faradaic region, and the corresponding double-layer capacitance (C_{dl}) values were obtained (Fig. S1(a–c)). As shown in Fig. 5(c), the fitted C_{dl} values for NiFc MOF, NiFc MOF@Mo_2CT_x, and S-NiFc MOF@Mo_2CT_x are 2.12, 2.30, and 2.74 mF cm^{-2}, respectively. According to the formula in Section 2.3, the corresponding electrochemical surface areas (ECSA) are calculated to be 13.3, 14.4, and 17.1 cm^2, indicating that the incorporation of Mo_2CT_x MXene and S-doping exposes more active sites in the S-NiFc MOF@Mo_2CT_x catalyst. Results from Fig. 5(d) confirm that S-NiFc MOF@Mo_2CT_x possesses higher electrochemical activity and ECSA-normalized activity, further illustrating the beneficial effects of sulfur doping and MXene support on enhancing the intrinsic activity of the NiFc MOF.

To further investigate the charge transfer capabilities of the catalysts, electrochemical impedance spectroscopy (EIS) was performed, and the corresponding Nyquist plots are shown in Fig. 5(e). The semicircle diameter in the high-frequency region represents the charge transfer resistance (R_{ct}), which is inversely correlated with the interfacial charge transfer rate. The R_{ct} values of S-NiFc MOF@Mo_2CT_x, NiFc MOF@Mo_2CT_x, and NiFc MOF are 7.84, 24.81, and 27.43 Ω, respectively, indicating that S-NiFc MOF@Mo_2CT_x possesses significantly improved charge transport capability. This enhancement arises from three synergistic factors: (1) the highly conductive Mo_2CT_x MXene provides continuous electron pathways, reducing interfacial resistance; (2) sulfur

doping induces electronic redistribution, enhancing interfacial activity and facilitating charge transfer; and (3) the three-dimensional open structure allows effective electrolyte penetration and active site exposure. Additionally, the lowest impedance of S-NiFc MOF@Mo_2CT_x is consistent with its excellent OER kinetics, further confirming its rapid interfacial electron transfer in practical electrolytic systems.

To visually compare the overall electrocatalytic performance of different catalysts, a radar chart was constructed based on five key indicators: overpotential at 10 mA cm^{-2}, overpotential at 100 mA cm^{-2}, Tafel slope, charge transfer resistance (R_{ct}), and electrochemical surface area (ECSA). As shown in Fig. 5(f), S-NiFc MOF@Mo_2CT_x performs best in all parameters, exhibiting the lowest overpotentials and Tafel slope, the smallest R_{ct}, and the largest ECSA. This highlights the synergistic effect of S doping and Mo_2CT_x support in enhancing interfacial electron transfer and exposing active sites, thereby promoting the oxygen evolution reaction kinetics. In contrast, although NiFc MOF@Mo_2CT_x benefits from the conductivity of the MXene substrate and performs better than NiFc MOF, it still falls short of S-NiFc MOF@Mo_2CT_x, underscoring the critical role of sulfur modulation in designing efficient OER catalysts.

Long-term durability is a crucial criterion in assessing the commercial viability of electrocatalysts. To this end, the stability of S-NiFc MOF@Mo_2CT_x was evaluated via *i–t* testing at an initial current density of 100 mA cm^{-2} in 1.0 M KOH using an electrochemical workstation. The catalyst suspension was coated onto a commercial titanium mesh (1×1 cm^2) as the working electrode to exclude possible performance contributions from surface oxidation of nickel foam during long-term stability tests. Notably, comparable initial performance was obtained on both titanium mesh and nickel foam, indicating that the substrate change did not influence the intrinsic activity. As shown in Fig. 5(g), S-NiFc MOF@Mo_2CT_x maintained stable operation over 68 h at 100 mA cm^{-2}, with a minor fluctuation reaching about 104 % of the initial current. This small variation is attributable to transient bubble effects and slight surface activation of the catalyst. Overall, this minor variation over prolonged electrolysis demonstrates the excellent long-term durability of the catalyst.

4. Conclusion

In this study, MOF-derived nickel–iron sulfide nanosheets (S-NiFc MOF@Mo_2CT_x) were successfully synthesized on a Mo_2CT_x MXene substrate via a simple two-step hydrothermal method. Electron microscopy characterization revealed that the NiFc MOF grows around the Mo_2CT_x core, forming a core–shell structure. This configuration not only prevents the restacking of Mo_2CT_x during the OER, but also enables full exposure of the active Ni and Fe sites to the electrolyte. XPS analysis confirmed that the Mo_2CT_x MXene serves as a rich charge transfer interface, promoting electron migration from Ni and Fe to the Mo_2CT_x substrate. This electronic redistribution lowers the electron cloud density around Ni and Fe, thereby accelerating the reaction kinetics. Moreover, sulfur doping further enhances the intrinsic activity of the catalyst. The activated S-NiFc MOF@Mo_2CT_x exhibits an ultralow overpotential (223 mV at 10 mA cm^{-2}) and a small Tafel slope (41.3 mV dec^{-1}), along with excellent stability, outperforming most reported powder-based NiFe OER catalysts and showing great promise for industrial applications.

CRediT authorship contribution statement

Pei-Wei Zhong: Writing – review & editing, Writing – original draft, Validation, Data curation. **Hong-Xiao Yang:** Methodology, Investigation, Data curation. **Wenkang Xu:** Formal analysis, Data curation. **Zhiyang Yu:** Formal analysis, Data curation. **Bei Li:** Formal analysis, Data curation. **Hongjuan Wang:** Writing – review & editing, Supervision. **Yonghai Cao:** Writing – review & editing, Supervision. **Hao Yu:** Writing – review & editing, Supervision. **Hao-Fan Wang:** Writing – review & editing, Supervision, Project administration, Funding acquisition.

Declaration of competing interest

The authors declare that they have no known competing financial interests or personal relationships that could have appeared to influence the work reported in this paper.

Acknowledgements

This work was financially supported by National Natural Science Foundation of China (grant No. 22209049) and Natural Science Foundation of Guangdong Province (grant Nos. 2023A1515012804, 2025A1515010003).

Appendix A. Supplementary data

Supplementary data to this article can be found online at https://doi.org/10.1016/j.partic.2025.12.020.

References

Abdelrahim, A. M., Abd El-Moghny, M. G., El-Shakre, M. E., & El-Deab, M. S. (2023). Double surface modification of graphite felt using a single facile step for electrolytic hydrogen production assisted by urea. *Electrochimica Acta, 440*, Article 141726. https://doi.org/10.1016/j.electacta.2022.141726

Ahn, S., Han, T. H., Maleski, K., Song, J. N., Kim, Y. H., Park, M. H., … Lee, T. W. (2020). A 2D titanium carbide MXene flexible electrode for high-efficiency light-emitting diodes. *Advanced Materials, 32*(23), Article 2000919. https://doi.org/10.1002/adma.202000919

Ali, A., & Shen, P. K. (2020). Recent progress in graphene-based nanostructured electrocatalysts for overall water splitting. *Electrochemical Energy Reviews, 3*(2), 370–394. https://doi.org/10.1007/s41918-020-00066-3

Connelly, N. G., & Geiger, W. E. (1996). Chemical redox agents for organometallic chemistry. *Chemical Reviews, 96*(2), 877–910. https://doi.org/10.1021/cr940053x

Gao, X. Q., Chen, Y. T., Wang, Y. J., Zhao, L. Y., Zhao, X. Y., Du, J., … Chen, A. B. (2024). Next-generation green hydrogen: Progress and perspective from electricity, catalyst to electrolyte in electrocatalytic water splitting. *Nano-Micro Letters, 16*(1), Article 237. https://doi.org/10.1007/s40820-024-01424-2

Gultom, N. S., Chen, T. S., Silitonga, M. Z., & Kuo, D. H. (2023). Overall water splitting realized by overall sputtering thin-film technology for a bifunctional MoNiFe electrode: A green technology for green hydrogen. *Applied Catalysis B: Environment and Energy, 322*, Article 122103. https://doi.org/10.1016/j.apcatb.2022.122103

Gaba, L., Siwach, P., Aggarwal, K., Dahiya, S., Punia, R., Maan, A. S., … Ohlan, A. (2024). Hybridization of metal-organic frameworks and MXenes: Expanding Horizons in supercapacitor applications. *Advances in Colloid and Interface Science, 332*, Article 103268. https://doi.org/10.1016/j.cis.2024.103268

Guo, B. Z., Kim, S. B., Lee, S. Y., & Park, S. J. (2025). Determination of surface free energy and acido-basicity of MXene materials measured by inverse gas chromatography at infinite dilution. *Carbon, 231*, Article 119732. https://doi.org/10.1016/j.carbon.2024.119732

Han, X. T., Yu, X., & Park, H. S. (2024). Recent advances in trifunctional electrocatalysts for Zn-air batteries and water splitting. *Materials Chemistry Frontiers, 8*(6), 1536–1562. https://doi.org/10.1039/d3qm01002c

Ji, J. L., Lou, W. H., & Shen, P. K. (2022). Modular design in metal-organic frameworks for oxygen evolution reaction. *International Journal of Hydrogen Energy, 47*(93), 39443–39469. https://doi.org/10.1016/j.ijhydene.2022.09.126

Kim, J. H., Youn, D. H., Kawashima, K., Lin, J., Lim, H., & Mullins, C. B. (2018). An active nanoporous Ni(Fe) OER electrocatalyst via selective dissolution of Cd in alkaline media. *Applied Catalysis B: Environmental, 225*, 1–7. https://doi.org/10.1016/j.apcatb.2017.11.053

Kim, J., Yu, J. M., Jang, W., Lee, J. Y., Kim, H., Kim, H., … Cho, S. H. (2024). Enhancing water oxidation catalysis by controlling metal cation distribution in layered double hydroxides. *Advanced Functional Materials, 34*(2), Article 2308902. https://doi.org/10.1002/adfm.202308902

Krämer, M., Favelukis, B., El-Zoka, A. A., Sokol, M., Rosen, B. A., Eliaz, N., … Gault, B. (2024). Near-atomic-scale perspective on the oxidation of Ti3C2Tx MXenes: Insights from atom probe tomography. *Advanced Materials, 36*(3), Article 2305183. https://doi.org/10.1002/adma.202305183. Article.

Kundu, A., Kuila, T., Murmu, N. C., Samanta, P., & Das, S. (2023). Metal-organic framework-derived advanced oxygen electrocatalysts as air-cathodes for Zn-air batteries: Recent trends and future perspectives. *Materials Horizons, 10*(3), 745–787. https://doi.org/10.1039/d2mh01067d

Lennox, A. J. J., Nutting, J. E., & Stahl, S. S. (2018). Selective electrochemical generation of benzylic radicals enabled by ferrocene-based electron-transfer mediators. *Chemical Science, 9*(2), 356–361. https://doi.org/10.1039/c7sc04032f

Li, Z. Q., Gao, R., Feng, M., Deng, Y. P., Xiao, D. J., Zheng, Y., … Chen, Z. W. (2021). Modulating metal-organic frameworks as advanced oxygen electrocatalysts. *Advanced Energy Materials, 11*(16), Article 2003291. https://doi.org/10.1002/aenm.202003291

Li, Li, J. P., Liu, X. X., & Guo, J. X. (2023a). Ir-doped Co-BDC MOF as efficient bifunctional catalyst for overall electrochemical water splitting. *Ionics, 29*(5), 1963–1973. https://doi.org/10.1007/s11581-023-04928-w

Li, Q. L., Li, X., Zhang, K., He, J. Q., Lou, Y. B., & Chen, J. X. (2023). Rod-like CoMoO4 grows on lamellar Fe-MOF to assemble the composite electrocatalyst for efficient oxygen evolution reaction. *Inorganic Chemistry Communications, 153*, Article 110835. https://doi.org/10.1016/j.inoche.2023.110835

Liang, J., Gao, X. T., Guo, B., Ding, Y., Yan, J. W., Guo, Z. X., … Liu, J. X. (2021). Ferrocene-based metal-organic framework nanosheets as a robust oxygen evolution catalyst. *Angewandte Chemie International Edition, 60*(23), 12770–12774. https://doi.org/10.1002/anie.202101878

Liu, Y. Z., Li, X. T., Zhang, S. F., Wang, Z. L., Wang, Q., He, Y. H., … Zhu, Z. L. (2023). Molecular engineering of metal-organic frameworks as efficient electrochemical catalysts for water oxidation. *Advanced Materials, 35*(22), Article 2300945. https://doi.org/10.1002/adma.202300945

Liu, S. L., Lin, Z. S., Wan, R. D. A., Liu, Y. G., Liu, Z., Zhang, S. D., … Tian, Y. (2021). Cobalt phosphide supported by two-dimensional molybdenum carbide (MXene) for the hydrogen evolution reaction, oxygen evolution reaction, and overall water splitting. *Journal of Materials Chemistry A, 9*(37), 21259–21269. https://doi.org/10.1039/d1ta05648d

Liu, S. J., Wei, Y., Wang, M. K., & Shen, Y. (2025). The future of alkaline water splitting from the perspective of electrocatalysts-seizing today's opportunities. *Coordination Chemistry Reviews, 522*, Article 216190. https://doi.org/10.1016/j.ccr.2024.216190

Liu, H., Xin, Z. J., Cao, B., Zhang, B., Fan, H. J., & Guo, S. J. (2024). Versatile MXenes for aqueous zinc batteries. *Advanced Science, 11*(8), Article 2305806. https://doi.org/10.1002/advs.202305806

Loupias, L., Morais, C., Morisset, S., Canaff, C., Li, Z. M., Brette, F., … Celerier, S. (2024). Guideline for synthesis and surface chemistry characterization of 2D Mo/Ti solid solutions based MXene. Application to hydrogen evolution reaction in alkaline media. *FlatChem, 43*, Article 100596. https://doi.org/10.1016/j.flatc.2023.100596

McCrory, C. C. L., Jung, S. H., Peters, J. C., & Jaramillo, T. F. (2013). Benchmarking heterogeneous electrocatalysts for the oxygen evolution reaction. *Journal of the American Chemical Society, 135*(45), 16977–16987. https://doi.org/10.1021/ja407115p

Meng, X. Y., Wei, Z. Y., Ma, L., Chen, R. F., Huang, X. X., He, P. G., … Duan, X. M. (2024). Synthesis of multilayered transition metal MOF/Ni3N/NF composites for efficient oxygen evolution reaction. *Journal of Alloys and Compounds, 1005*, Article 176142. https://doi.org/10.1016/j.jallcom.2024.176142

Mohideen, M. M., Santhosh, P. C., Radhamani, A. V., Wang, C., Hu, P., Subramanian, B., … Liu, Y. (2026). Negative impact of sulfur doping on ORR/OER performance in dual-active-site Co-MOF/MXene electrocatalysts. *Journal of Colloid and Interface Science, 703*, Article 139165. https://doi.org/10.1016/j.jcis.2025.139165

Nozari-Asbemarz, M., Imanzadeh, H., Hazraty, L., Babaei, B., Abbasi, A., Mehrabi-Kalajahi, S. S., … Amiri, M. (2025). Construction of iron-nickel metal-organic framework anchored on reduced graphene oxide for enhanced oxygen evolution reaction electrocatalysis. *Journal of Power Sources, 652*, Article 237555. https://doi.org/10.1016/j.jpowsour.2025.237555

Pazhamalai, P., Krishnamoorthy, K., Swaminathan, R., Natraj, V., & Kim, S. J. (2024). Unravelling the trifunctional electrochemical properties of WSe2 nanosheets for self-powered hydrogen production. *Nano Energy, 120*, Article 109084. https://doi.org/10.1016/j.nanoen.2023.109084

Peng, C., Zhou, T., Wei, P., Xu, W. K., Pan, H., Peng, F., … Yu, H. (2021). Photocatalysis over MXene-based hybrids: Synthesis, surface chemistry, and interfacial charge kinetics. *APL Materials, 9*(7), Article 070703. https://doi.org/10.1063/5.0055711

Qi, J., Zhang, W., & Cao, R. (2018). Solar-to-Hydrogen energy conversion based on water splitting. *Advanced Energy Materials, 8*(5), Article 1701620. https://doi.org/10.1002/aenm.201701620

Qi, Q. L., Zhang, Y., Zhang, C. X., Liu, F., Liu, R. J., & Hu, J. (2024). Halogen-modified iron-based metal-organic frameworks for remarkably improved electrocatalytic oxygen evolution. *Journal of Physical Chemistry C, 128*(5), 1936–1945. https://doi.org/10.1021/acs.jpcc.3c06800

Qiu, S. P., Hao, S. H., Xing, Y. P., Huang, J. Z., Wang, X., Ding, M., … Zhang, Y. F. (2022). Adjusting electronic structure coupling of Fe-Ni2P (NiFeP-MOF) multilevel structure for ultra-activity and durable catalytic water oxidation. *International Journal of Hydrogen Energy, 47*(71), 30472–30483. https://doi.org/10.1016/j.ijhydene.2022.07.013

Quiroz, S. G., Cartagena, S., & Calderón, J. A. (2025). Enhancement of oxygen evolution performance of water splitting at high current density by novel electrodeposited NiFe-LDH coatings. *Electrochimica Acta, 528*, Article 146332. https://doi.org/10.1016/j.electacta.2025.146332

Radwan, A., Jin, H. H., He, D. P., & Mu, S. C. (2021). Design engineering, synthesis protocols, and energy applications of MOF-derived electrocatalysts. *Nano-Micro Letters, 13*(1), Article 132. https://doi.org/10.1007/s40820-021-00656-w

Salles, P., Pinto, D., Hantanasirisakul, K., Maleski, K., Shuck, C. E., & Gogotsi, Y. (2019). Electrochromic effect in titanium carbide MXene thin films produced by dip-coating. *Advanced Functional Materials, 29*(17), Article 1809223. https://doi.org/10.1002/adfm.201809223

Shahzad, F., Iqbal, A., Kim, H., & Koo, C. M. (2020). 2D transition metal carbides (MXenes): Applications as an electrically conducting material. *Advanced Materials, 32*(51), Article 2002159. https://doi.org/10.1002/adma.202002159

Shi, M. J., Sultana, F., Qin, X. J., Zhang, P., Qian, K. C., Wei, T., … Li, R. H. (2025). In situ evolution of MOF-Derived C@NiCoP/NF promotes urea-assisted electrocatalytic hydrogen production. *Applied Catalysis B: Environment and Energy, 371*, Article 125210. https://doi.org/10.1016/j.apcatb.2025.125210

Sondermann, L., Jiang, W., Shviro, M., Spiess, A., Woschko, D., Rademacher, L., & Janiak, C. (2022). Nickel-based metal-organic frameworks as electrocatalysts for the oxygen evolution reaction (OER). *Molecules, 27*(4), Article 1241. https://doi.org/10.3390/molecules27041241

Sun, Y. W., Li, Z. Q., Sun, B., Mao, Y. Y., Huang, B. B., & Cheng, H. F. (2024). High-performance artificial leaf: From electrocatalyst design to solar-to-chemical conversion. *Materials Chemistry Frontiers, 8*(5), 1300–1333. https://doi.org/10.1039/d3qm01179h

Tang, M. R., Li, J. M., Wang, Y., Han, W. J., Xu, S. C., Lu, M., … Li, H. B. (2022). Surface terminations of MXene: Synthesis, characterization, and properties. *Symmetry-Basel, 14*(11), Article 2232. https://doi.org/10.3390/sym14112232. Article.

Tang, J., Mathis, T. S., Kurra, N., Sarycheva, A., Xiao, X., Hedhili, M. N., … Gogotsi, Y. (2019). Tuning the electrochemical performance of titanium carbide MXene by controllable in situ anodic oxidation. *Angewandte Chemie International Edition, 58*(49), 17849–17855. https://doi.org/10.1002/anie.201911604

Unnikrishnan, B., Wu, C. W., Sangili, A., Hsu, Y. J., Tseng, Y. T., Pandey, J. S., … Huang, C. C. (2022). Synthesis and in situ sulfidation of molybdenum carbide MXene using fluorine-free etchant for electrocatalytic hydrogen evolution reactions. *Journal of Colloid and Interface Science, 628*, 849–857. https://doi.org/10.1016/j.jcis.2022.07.176

Wang, M. Y., Srinivas, K., Liu, D. W., Yu, H. S., Ma, F., Zhang, Z. H., … Chen, Y. F. (2024). Metal-organic framework-derived Fe/NiS heterostructure-embedded nanosheets coupled with carbon nanotubes for excellent oxygen evolution reaction. *Journal of Alloys and Compounds, 972*, Article 172709. https://doi.org/10.1016/j.jallcom.2023.172709

Wang, B., Tang, C., Wang, H. F., Chen, X., Cao, R., & Zhang, Q. (2019a). Core-branch CoNi hydroxysulfides with versatilely regulated electronic and surface structures for superior oxygen evolution electrocatalysis. *Journal of Energy Chemistry, 38*, 8–14. https://doi.org/10.1016/j.jechem.2018.12.006

Wang, B., Tang, C., Wang, H. F., Chen, X., Cao, R., & Zhang, Q. (2019b). A nanosized CoNi hydroxide@hydroxysulfide core-shell heterostructure for enhanced oxygen evolution. *Advanced Materials, 31*(4), Article 1805658. https://doi.org/10.1002/adma.201805658

Wu, T., Sun, M. Z., & Huang, B. L. (2022). Non-noble metal-based bifunctional electrocatalysts for hydrogen production. *Rare Metals, 41*(7), 2169–2183. https://doi.org/10.1007/s12598-021-01914-x

Wu, Y., Xiao, B. X., Liu, K. L., Wang, S. B., Hou, Y. D., Lu, X. F., & Zhang, J. J. (2025). Electrochemical synthesis of high-efficiency water electrolysis catalysts. *Electrochemical Energy Reviews, 8*(1), Article 2. https://doi.org/10.1007/s41918-024-00237-6

Xie, X. Y., Zhai, Z. Y., Peng, L. S., Zhang, J. B., Shang, L., & Zhang, T. R. (2023). Recent advances in bifunctional dual-sites single-atom catalysts for oxygen electrocatalysis toward rechargeable zinc-air batteries. *Science Bulletin, 68*(22), 2862–2875. https://doi.org/10.1016/j.scib.2023.10.013

Xing, D. N., Wang, H. X., Cui, Z., Lin, L. T., Liu, Y. Y., Dai, Y., & Huang, B. B. (2024). A conductive two-dimensional trimetallic FeCoNi-Benzenehexathiol π-d conjugated metal-organic framework for highly efficient oxygen evolution reaction. *Journal of Colloid and Interface Science, 656*, 309–319. https://doi.org/10.1016/j.jcis.2023.11.104

Xu, W. K., Shi, Z. A., Yu, Z. Y., Peng, C., Yang, G. X., Wang, H. F., … Yu, H. (2024). A sweet synthesis of MXenes. *Nano Letters, 24*(34), 10547–10553. https://doi.org/10.1021/acs.nanolett.4c02584

Zhang, Cao, C. T., Ling, T., Ye, C., Lu, J., & Shan, J. Q. (2024a). Developing practical catalysts for high-current-density water electrolysis. *Advanced Energy Materials, 14*(45), Article 2402633. https://doi.org/10.1002/aenm.202402633

Zhang, Y. X., Zou, J., Wang, S. J., Hu, X. S., Liu, Z. H., Feng, P. Y., … Liu, Y. J. (2024). Tailoring nanostructured MXene to adjust its dispersibility in conductive hydrogel for self-powered sensors. *Composites Part B-Engineering, 272*, Article 111191. https://doi.org/10.1016/j.compositesb.2024.111191

Zhao, C. X., Liu, J. N., Wang, C. D., Wang, J., Song, L., Li, B. Q., & Zhang, Q. (2022). An anionic regulation mechanism for the structural reconstruction of sulfide electrocatalysts under oxygen evolution conditions. *Energy & Environmental Science, 15*(8), 3257–3264. https://doi.org/10.1039/d2ee01036d

Zhong, H. X., Wang, M. C., Chen, G. B., Dong, R. H., & Feng, X. L. (2022). Two-Dimensional conjugated metal-organic frameworks for electrocatalysis: Opportunities and challenges. *ACS Nano, 16*(2), 1759–1780. https://doi.org/10.1021/acsnano.1c10544

Zhu, R. M., Liu, L. M., Zhang, G. X., Zhang, Y., Jiang, Y. X., & Pang, H. (2024). Advances in electrochemistry of intrinsic conductive metal-organic frameworks and their composites: Mechanisms, synthesis and applications. *Nano Energy,, 122*, Article 109333. https://doi.org/10.1016/j.nanoen.2024.109333

Zhuo, Y. L., Liu, D., Qiao, L. L., Chen, S. B., Lu, J. X., Ip, W. F., … Wang, Z. B. (2023). Ultrafast room-temperature synthesis of large-scale, low-cost, and highly active Ni-Fe based electrodes toward industrialized seawater oxidation. *Advanced Energy Materials, 13*(39), Article 2301921. https://doi.org/10.1002/aenm.202301921

Zong, M., Wang, K. K., Lin, Z. S., & Tang, Z. H. (2021). Phosphorylated NiCo metal-organic-frameworks for efficient oxygen evolution reaction. *International Journal of Electrochemical Science, 16*(9), Article 21094. https://doi.org/10.20964/2021.09.22